Appl Phys A (2011) 103: 335–341
DOI 10.1007/s00339-010-6152-8

Applied Physics A
Materials Science & Processing

Effect of built-in electric field in photovoltaic InAs quantum dot embedded GaAs solar cell

X.J. Shang · J.F. He · H.L. Wang · M.F. Li · Y. Zhu · Z.C. Niu · Y. Fu

Received: 24 September 2010 / Accepted: 30 November 2010 / Published online: 21 December 2010

Abstract In this paper, three p–i–n GaAs solar cells were grown and characterized, one with InAs quantum dot (QD) layers embedded in the depletion region (sample A), one with QD layers embedded in the n^- base region (B), and the third without QDs (control sample C). QD-embedded solar cells (samples A and B) show broad photoluminescence spectra due to QD multi-level emissions but have lower open-circuit voltages V_{oc} and lower photovoltaic (PV) efficiencies than sample C. On the other hand, the short-circuit current density J_{sc} in sample A is increased while it is decreased in sample B. Theoretical analysis shows that in sample B where the built-in electric field in QDs is zero, electrons tend to occupy QDs and strong potential variations exist around QDs which deteriorate the electron mobility in the n^- base region so that J_{sc} in sample B is decreased. Hole trapping and electron–hole recombination in QDs are also enhanced in sample B, resulting in a reduced V_{oc} and thus a worse PV effect. In sample A, a strong built-in field exists in QD layers, which facilitates photo-carrier extraction from QDs and thus J_{sc} is increased. However, QDs in the depletion region in sample A act also as recombination-generation centers so that the dark saturated current density is drastically increased, which reduces V_{oc} and the total PV effect. In conclusion, a nonzero built-in electric field around QDs is vital for using QDs to increase the PV effect in conventional p–i–n GaAs solar cells.

X.J. Shang (✉) · J.F. He · H.L. Wang · M.F. Li · Y. Zhu · Z.C. Niu
State Key Laboratory for Superlattices and Microstructures,
Institute of Semiconductors, Chinese Academy of Sciences,
P.O. Box 912, Beijing 100083, China
e-mail: xjshang@semi.ac.cn

X.J. Shang · Y. Fu
Department of Theoretical Chemistry, School of Biotechnology,
Royal Institute of Technology, 106 91 Stockholm, Sweden

Y. Fu
e-mail: fyg@theochem.kth.se

1 Introduction

Quantum dot (QD) embedded solar cells have been extensively studied due to their potential to increase photovoltaic (PV) conversion efficiency based on multiple exciton generation (MEG) [1–3] and/or additional intermediate band (IB) absorption [4–7]. The MEG effect, mostly in colloidal QDs, is a mechanism that one high-energy photon produces two or more electron–hole (e–h) pairs in QDs via impact ionization. The IB mechanism, on the other hand, recycles sub-band-gap photons via additional multi-step photon absorption through IBs formed by QD layers. Though little evidence shows the MEG effect in epitaxial InAs QDs, their IB effect has been well demonstrated in the form of sub-band-gap quantum efficiencies [8–12].

The most common structure of epitaxial InAs QD solar cells is a p–i–n framework with InAs QD layers embedded in the i (intermediate) region [13]. Note that an i-region in a semiconductor device normally refers to an intrinsic and/or undoped region, whereas in this work we denote it to be the whole intermediate region with low doping levels between two highly doped n and p contact layers. It includes the undoped layer and an n^- base layer (see more discussion below). The i-region, serving as the main active part of a solar cell, is usually designed wide enough for efficient light absorption. Within this region, QDs can be positioned close to the p-contact layer [8, 9], the n-contact layer [11], or in the middle of the i-region [14]. Photo-carriers from QDs are extracted via electric-field-induced tunneling as in QD infrared photodetectors [15], thermal escape [16], or multi-step photon absorption as expected by the IB concept [7].

Since these QD IBs are disconnected from the band states in the two contacts, the IB absorption is expected to increase the photo-current while at the same time keep the photo-voltage unchanged [10].

In this work, three types of GaAs solar cells were grown and characterized. Sample A has five InAs QD layers embedded in the depletion region while, in sample B, QD layers are embedded in the flat-band n^- base region, and sample C does not contain any QDs (the control sample). The major difference between samples A and B is in the electric field strengths across QDs. In sample A, QDs are positioned in the depletion layer where a strong built-in electric field exists, while the average electric field across the QDs in the n^- base layer in sample B is zero. Note that our sample structures are very similar to others in the literature [8, 9, 11, 13, 14], while the major aim of this work is to investigate and show the dominant role of the electric field in the photo-carrier extraction from QDs that determines the overall PV efficiency of the InAs-QD-embedded GaAs solar cell.

The device design and fabrication are described in Sect. 2. In Sect. 3, photoluminescence (PL) spectra and PV measurements are presented to characterize our cells. Energy band structures of the three cells are theoretically calculated to analyze experimental data in Sect. 4, followed by a brief summary in Sect. 5.

2 Design and fabrication of our cells

Figure 1 shows schematically the structures of our three cells, whose main parts are p–i–n structures in GaAs. The p and n GaAs contact layers are 500 nm each, and Be doped at 2×10^{17} cm^{-3} and Si doped at 1×10^{18} cm^{-3}, respectively. Between them is a 2-μm-thick i-region composed of two layers, a low-doped (Si 2×10^{16} cm^{-3}) 1860-nm n^- base layer and an undoped 140-nm depletion layer to sustain the built-in field as well as to suppress Be-diffusion-induced dark current. Low doping levels are adopted in both the p-type emitter and the n^- base for better diffusion of photo-generated minority carriers [17].

The built-in field region (i.e. the depletion region) is thick enough to cover the five QD layers in sample A (see Fig. 4 and more discussion in Sect. 4) in order to utilize the built-in electric field in the depletion region to drive and extract photo-carriers in QDs. This is our basic scheme for sample A.

As for sample B, three groups of five QD layers are positioned in the flat-band n^- base layer separated by 488-nm-thick GaAs layers to minimize dislocations. In the flat-band n^- base layer, photo-carriers generated in QDs by the IB absorption are expected to be extracted by either thermal escape or multi-step photon absorption [11]. It provides a direct means to test the IB effect since QDs are required to be put in a flat-band region to ensure that IBs are half-filled everywhere [18].

Furthermore, a top window layer of 100-nm-thick p-type $Al_{0.85}Ga_{0.15}As$ and a back surface field layer of 100-nm n-type $Al_{0.2}Ga_{0.8}As$ are introduced to prevent minority photo-carriers diffusing into the surfaces and to reduce the surface recombination, as commonly practiced in conventional bulk material solar cells [19].

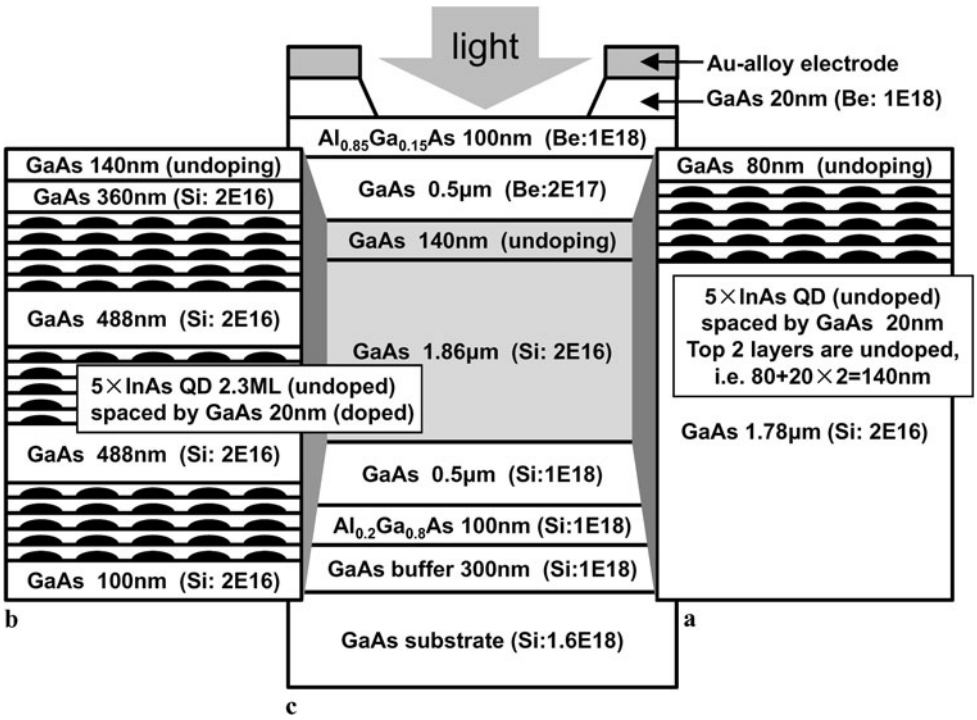

Fig. 1 Schematic structures of the three p–i–n GaAs solar cells under investigation. (**a**) *Sample* A: five InAs QD layers spaced by 20-nm GaAs layers embedded in the depletion region; (**b**) *sample* B: three groups of five QD layers embedded in the n^- base region; (**c**) *sample* C: non-QD control sample

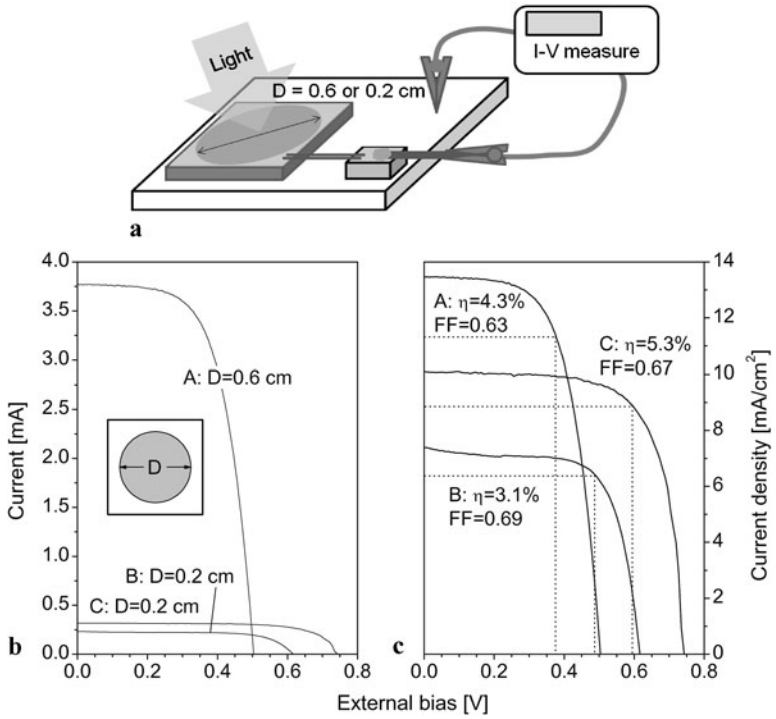

Fig. 2 (**a**) Schematic QD solar cell structure and measurement setup. (**b**) Photo-current and (**c**) photo-current density as functions of the external bias voltage, i.e. the I–V characteristics under light. D is the diameter of the light-absorption area, η the PV efficiency, and FF the fill factor. Solar-simulator light intensity is calibrated by a standard Si solar cell to about 1 sun AM1.5G

All three samples were grown on n^+-doped GaAs crystal wafers by Veeco Gen II molecular beam epitaxy (MBE). First, the temperature of the wafer was raised to about 620°C and kept for about 10 min to desorb surface oxygen. The wafer temperature was then cooled to 600°C for the following solar cell structure growth. A 300-nm-thick GaAs buffer with a doping level of 1×10^{18} cm^{-3} was grown to smooth the growth surface. AlGaAs and GaAs layers in the cell structure were grown at 600°C, while the QD matrices including self-assembled 2.3 monolayers (ml) InAs QDs and the 20-nm GaAs spacer layers were grown at 500°C. InAs was deposited at a slow rate of 0.1 ml/s plus a 10-s interrupt after every 0.1 ml, and the As/In flux ratio was set to be 15:1. The slow deposition rate and the proper As/In flux ratio are to ensure sufficient movements of InAs molecules on the growth surface and thus the size uniformity of QDs. The 2.3 ml deposition amount was optimized to form QDs with the proper size and correct sheet density after island formation at 1.8 ml. The As flux was open all the time through the whole growth process to avoid As-atom desorption. In our MBE system, Si and Be were used as the donor and acceptor dopants, respectively. The whole process of QD formation is monitored by reflection high-energy electron diffraction.

After the MBE growth, a top CrAu electrode was evaporated and metalized followed by photolithography and wet etching that form the light-absorption area. Samples were then thinned down to about 130-μm thick from the back side on which a back AuGeNi electrode was evaporated and metalized. Finally, the back electrode was pasted with an indium layer on a standard heat sink while the top electrode was connected with metal wires to a base which is insulated from the heat sink, as shown in Fig. 2a. These cells are not coated with anti-reflection films, since we focus on comparing and exploring the PV effect of QDs in the p–i–n GaAs solar cells. The light-absorption areas are circular with a diameter of 0.6 cm for sample A and 0.2 cm for samples B and C.

3 Device characterization

In this section, the bias-dependent PL spectrum and the solar simulator based PV measurement results are presented. A He–Ne laser was used as the pump light for PL measurements. Devices are mounted on an insulating base and connected to a constant-voltage source meter. The measurements were performed at room temperature (RT, 300 K) and the results are presented in Fig. 3. Different voltages ranging from –1.0 V to +1.0 V were used to explore the dependence of QD radiative recombination on the electric field across the QDs.

Figure 3a shows that the PL peak intensity of sample A increases as the forward bias voltage increases from 0.0 to 1.0 V. This is because the built-in field in the depletion region is reduced by the forward bias, which makes the photo-carrier extraction from QDs more difficult, resulting in an enhanced e–h recombination in QDs. The backward bias condition (even a bias as low as –0.1 V here) can significantly increase the built-in field and facilitate photo-carrier

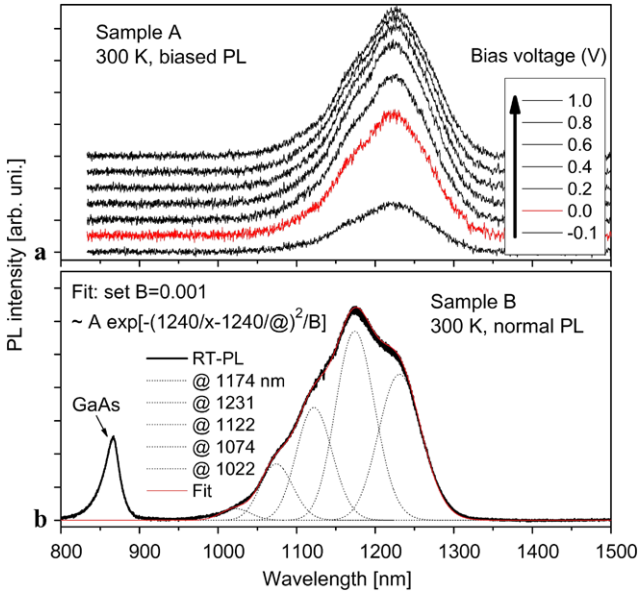

Fig. 3 (**a**) Bias-dependent RT-PL spectra of sample A. (**b**) RT-PL spectrum of sample B without external bias. Dotted lines indicate different QD energy levels or IBs that are fitted by Gaussian profiles. The red line gives the sum of these fit lines, showing a good agreement with the measured PL

extraction so that the PL intensity is much reduced. A similar measurement was performed on sample B, whose PL spectrum does not show a clear bias dependence. This can be expected, since the external bias applies in the depletion region while QD layers in sample B are located in the flat-band n^- base region.

Figure 3b shows the unbiased PL spectrum of sample B. Dotted lines represent different QD emission peaks, which are fitted by Gaussian profiles with the center wavelengths starting as '@'. The measured PL is well fitted with the sum of these dotted lines (i.e. the red line in this figure). There are at least five emission peaks from 1022 nm to 1231 nm, corresponding to five levels (IBs) in the QD assembly. Similar IB levels are obtained from the PL spectra of sample A. The average sheet density of our QDs is 300 μm^{-2} obtained from atomic force microscopy characterization. Dividing this sheet density by the spacer thickness of 20 nm gives us a three-dimensional QD density of 1.5×10^{16} cm^{-3}. By assuming five IB levels per QD as shown in Fig. 3b, we obtain an IB density of 7.5×10^{16} cm^{-3}. Since the Si doping level in the n^- region is 2×10^{16} cm^{-3}, we conclude that IBs in sample B are partially filled with electrons, exactly as required by the IB mechanism [18]. These five IB levels (in a wavelength range of 1022–1231 nm, i.e. 1.009–1.216 eV) are enough to recycle sub-band-gap photons (i.e. $1\ \text{eV} < h\nu < 1.424$ eV, where 1.424 eV is the GaAs band gap and $h\nu$ denotes photon energy) and thus are expected to enhance the PV effect [6] under the condition that photo-carriers occupying these IB levels can be extracted rapidly from QDs before they recombine. Otherwise, these levels will act as recombination channels for photo-carriers and reduce the overall PV effect.

The PL intensity of sample A is much stronger than sample B, although the total number of QDs in sample B is three times that in sample A. Furthermore, PL peaks in sample B are slightly blue shifted with respect to sample A. They are most probably related to the strain relaxations and dislocations in multiple QD layers of sample B. As the number of QD layers increases, the strain in each QD layer is gradually relaxed due to the strain redistribution in GaAs spacers [20]. Strain also relaxes in the form of dislocations [9]. On the relaxed growth surface, InAs islands are delayed to form and the final QDs are flat, which increases the quantum confinement in QDs and leads to the observed blue shift in the PL spectrum. Various dislocations in multiple QD layers degrade the luminescence properties of the QDs, so that the total PL intensity of sample B becomes weak.

These PL results support consistently our major conclusion that the built-in field distribution is critical for InAs QDs to enhance the PV effect in p–i–n GaAs solar cells.

PV measurements of our three cells were performed under a solar simulator (a xenon lamp) with the intensity of 1 sun AM1.5G (100 mW/cm^2), which was calibrated by a standard Si solar cell. Samples were located at a fixed position in a box with black internal walls and the xenon lamp on the top so the input light to the samples comes directly from the lamp, not from diffused light. The I–V meter, located outside the box with two wires connected separately to the two electrodes of a sample, supplies a scanning voltage and records the corresponding current in time until the photo-current reaches zero. The measurement was also performed at room temperature.

The I–V characteristics under light of the three samples are presented in Fig. 2b and c. Compared with sample C, the two QD solar cells, A and B, have lower open-circuit voltages (V_{oc}). Moreover, sample A has the highest short-circuit current density (J_{sc}) (about 1/3 higher than sample C), while sample B has the lowest one (about 1/3 less). The PV efficiencies of both A and B are lower than C, while B has the lowest one. The fill factor, FF, of sample A is lower than B and C. As aforementioned, we focus on the relative performance of the three cells, so that the absolute PV efficiencies are not compared with other works in the literature.

The simplest equivalent description of a solar cell can be expressed as [17]

$$J = J_{sc} - J_0\left(e^{qV/nk_BT} - 1\right). \quad (1)$$

Here J_{sc} is the short-circuit photo-current density, while J_0 is the dark saturated current density, n the ideality factor, V the bias between two contacts, q the charge unit, k_B the Boltzmann constant, and T the absolute temperature. We

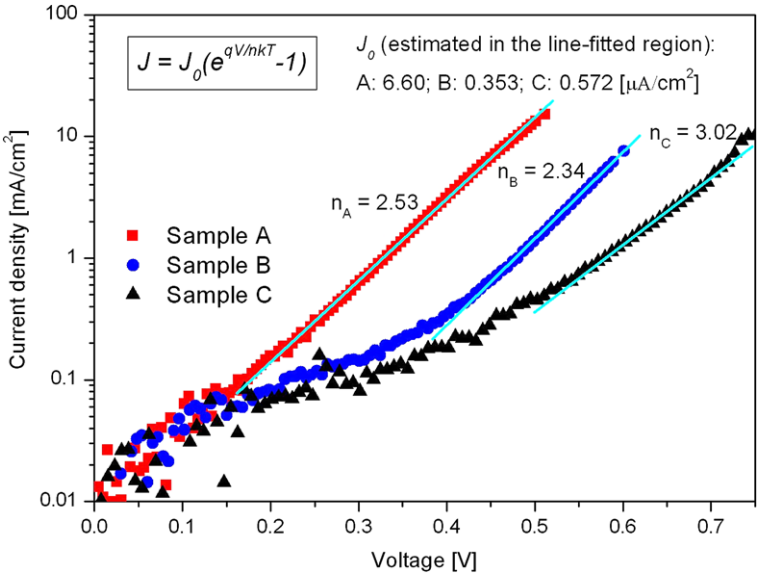

Fig. 4 Diode performances of our three solar cells. Here, the current density is obtained by extracting the measured photo-current J in Fig. 2c by J_{sc}. The ideality factor n and the dark saturated current density J_0 are estimated in the line-fitted region

can easily obtain

$$V_{oc} = (nk_BT/q)\ln(J_{sc}/J_0 + 1) \tag{2}$$

from (1) by letting $J = 0$.

As noticed by (1), the diode performances of our three samples can be obtained by extracting their respective J_{sc}, which are presented in Fig. 4. The introduction of QDs in sample B induces strong potential variations in the flat-band n^- base region (see more discussion in Sect. 4), which reduce the electron mobility. Both J_0 and J_{sc} are thus reduced proportionally so that the J_{sc}/J_0 ratio remains basically unchanged. The ideality factor n in sample B is smaller than sample C, so that V_{oc} is reduced. The reduced J_{sc} and V_{oc} degrade greatly the final PV efficiency of sample B.

As shown in Fig. 4, J_0 of sample A is about 10 times that of sample C. This can be understood by the fact that the depletion region in sample A is embedded with QDs which act not only as photon absorbers (responsible for the $1/3$ enhancement in J_{sc}, see more discussion below) in the short-circuit condition, but also as carrier traps and recombination centers near the open-circuit condition. Since J_{sc} is only increased by $1/3$ while J_0 is increased by one order, apart from the slight reduction of n, $\ln(J_{sc}/J_0 + 1)$ is quite reduced, giving a much reduced V_{oc} and the final reduced PV efficiency in sample A.

4 Theoretical analysis

In this section, we calculate energy band structures of the three samples in order to analyze and understand their device performance in terms of the built-in field in the depletion region and the local potential variations in the n^- base region.

The devices are approximated as one dimensional (1D), where each InAs QD layer is approximated by an effective InAs quantum well in thickness of 0.7 nm, i.e. 2.3 ml, along the sample growth direction, which is denoted as the z axis. The densities of electron and hole states in such a quantum well are approached by delta functions of energy levels obtained from Fig. 3 to account for the discrete nature of QD levels [21, 22]. The calculated 1D band structures are shown in Fig. 5.

In the band diagram of sample A (Fig. 5a, under the short-circuit condition), the five QD layers in the depletion region are almost empty (depleted) due to the built-in field there, leading to efficient photo-carrier extraction from these QDs. Extra photo-carriers generated in QDs by near-infrared photon absorption (i.e. 1.0 eV $< h\nu <$ 1.424 eV) are easily extracted by the built-in field as shown in Fig. 6a, resulting in an increased J_{sc} as compared with sample C (control sample without QDs).

For sample B shown in Fig. 5b, the three groups of the QD layers are located in the flat-band n^- base. Majority electrons from donors in the n-doped GaAs occupy these QDs easily that form strong local potential variations around QDs and degrade the electron mobility in the conduction band [23]. Moreover, these potential variations serve as energy wells to trap photo-generated minority holes into QDs, making them easily recombine (both radiatively and nonradiatively) with the majority electrons already occupying the QDs, as shown in Fig. 6b. Both effects deteriorate the PV effect in sample B. Since such potential variations in the n^- base layer remain exactly the same in short-circuit and open-circuit conditions, both J_{sc} and V_{oc} of sample B are reduced, resulting in the lowest overall PV efficiency.

For sample A in the open-circuit condition, the built-in field is reduced due to the output photo-voltage so that the

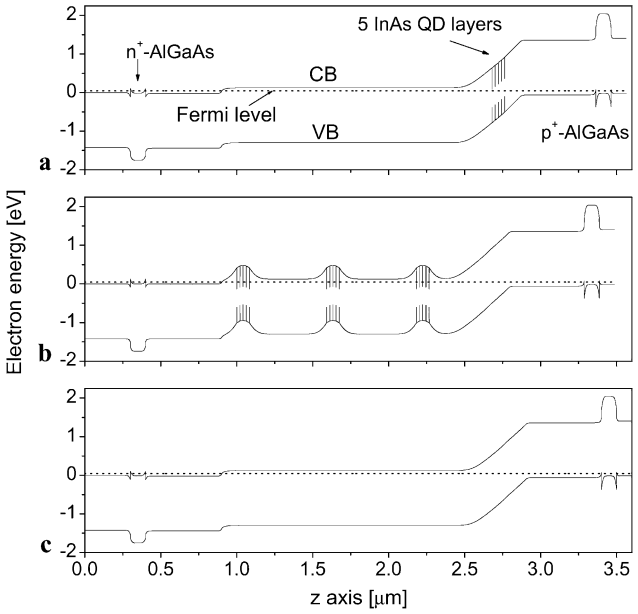

Fig. 5 One-dimensional energy band diagrams of our cells. (**a**) Sample A; (**b**) B; and (**c**) C. In each figure, solid lines represent the conduction band (CB) and valence band (VB) edges, respectively, while the dotted line denotes the Fermi level. On each side, the doped AlGaAs layer enables the minority photo-carriers to pass through while reflecting the majority ones selectively to produce photo-current, e.g. the *n*-doped AlGaAs layer enables electrons pass to the left, while it reflects holes back to the right

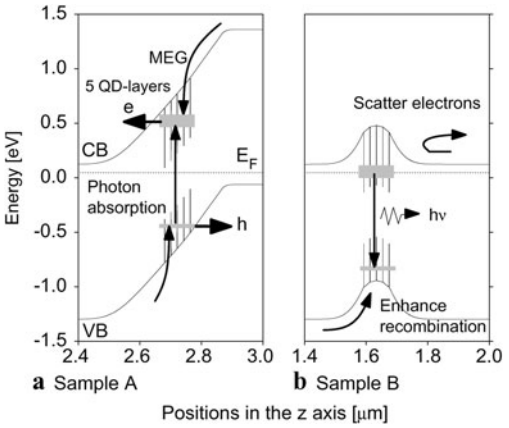

Fig. 6 (**a**) Near-infrared photon absorption and built-in electric field induced tunneling to explain the increased J_{sc} in sample A. (**b**) Local potential variations enhance the recombination and reduce the electron mobility. Both of them reduce the overall PV effect.

field-induced photo-carrier extraction from QDs becomes difficult. Photo-carrier recombination in QDs in the depletion region is enhanced, giving a drastically increased J_0 and thus a much reduced V_{oc}. The increase of J_{sc} is counteracted by the reduction in V_{oc}, resulting in a reduced PV efficiency. In order to minimize the V_{oc} reduction and to increase the PV efficiency, the built-in field near the open-circuit condition must be increased by improving structure design for photo-carrier extraction.

Though the light input is not included in the band-structure calculation, the above 1D band structures are still valid since the photo-carrier density is much less than the doping levels in our cells. By approximating the solar spectrum as a black-body emission at 5500 K with a total power density of 100 mW/cm^2 (our solar simulator used in the device characterization), there are about 3.6×10^{17} photons incident per second into 1 cm^2 of a cell surface. Assuming that the lifetime of photo-carriers is 1 ns (1.74 ns determined by the time-resolved PL decay time [19]) and the average absorption coefficient is 1 μm^{-1} (though it depends on the wavelength and materials and, for GaAs, it is 0.5 μm^{-1} at 870 nm and 2 μm^{-1} at 600 nm [17]), the maximal photo-carrier density is about 10^{12} cm^{-3}, which is negligible compared to the doping level of 2×10^{16} cm^{-3}.

The input solar photons of about 3.6×10^{17} per second can be divided into three parts by the absorption limits of GaAs bulk (867 nm) and InAs QDs (1300 nm as shown in Fig. 3): 2.1×10^{17} with wavelengths less than 867 nm, 8×10^{16} between 867 and 1300 nm, and 7×10^{16} with wavelengths longer than 1300 nm. The first part is expected to be absorbed by GaAs, while the second part is expected to be recycled by InAs QDs. The rate between the second and the first parts agrees with the 1/3 increase of J_{sc} in sample A as compared with sample C.

However, the PV conversion enhancement via the IB effect (by either multi-step photon absorption or thermal escape) is not found in sample B, as similarly reported in the literature [8], though it was reported that sub-band-gap photons should show significant quantum efficiencies [8, 10]. We believe by our work that the main problems here are the photo-carrier trapping and recombination in QDs located in the flat-band n^- base region.

The calculation in [13] also showed an increased J_{sc} from 35.1 to 45.17 mA/cm^2, in agreement with our result of the 1/3 increase. However, it showed only a slightly reduced V_{oc} (from 0.753 to 0.746 V) for QD solar cells, while our experimental work shows a much greater V_{oc} reduction from 0.75 to 0.5 V. It is believed that the difference is due to the neglect of the QD carrier-trapping effect in [13], where all photo-carriers are assumed to be extracted from QDs in both the short-circuit and open-circuit conditions. In fact, effective photo-carrier extraction is not realistic under the open-circuit condition because of the enhanced carrier trapping and recombination in QDs. A similar large V_{oc} reduction was also shown in [14].

Moreover, the growth of self-assembled InAs QDs is based on the misfit strains which can accumulate in close-stacked multiple QD layers and introduce dislocations in the top p^+ emitter. These dislocations are centers of Auger recombination, which can degrade the PV performance. It was reported that increasing the number of QD layers degrades

the overall PV effect in a QD cell [9]. This is consistent with our work that sample B has a lower PV efficiency than sample A.

5 Conclusion

In a brief summary, three p–i–n GaAs solar cells, two with InAs QDs embedded in different regions and one without QDs, were grown to investigate the role of the built-in electric field in the QD solar cell. Compared to the control sample C (without QDs), QD-embedded solar cells, samples A and B, have lower open-circuit voltages V_{oc} due to the carrier trapping and recombination enhancement in QDs. The short-circuit current density J_{sc} of sample B (where the QDs are embedded in the n^- base region) is also reduced for the same reason, while that of sample A with QDs embedded in the depletion region is increased since additional photocarriers generated by sub-band-gap photon absorption are extracted from QDs by the strong built-in field. As a whole, both A and B have lower PV efficiencies than C, while B has the lowest one. Apart from the above-mentioned reasons, QD-induced dislocations are also possible causes of the reduced PV effect. In all, the geometry of sample A (QDs embedded in the depletion region) has the potential to increase PV efficiency if a strong built-in field is formed by improving the structure design for enhancing photo-carrier extraction near the open-circuit condition and thus minimizing V_{oc} reduction.

Acknowledgements The work was partially financially supported by the Chinese Natural Science Fund (Grant No. 60625405) and the 973 project (Grant No. 2010CB327601) in China, the Richertska Foundation in Sweden, and the Swedish National Infrastructure for Computing (SNIC 001-09-52).

References

1. A.J. Nozik, Physica E **14**, 115 (2002)
2. R.D. Schaller, J.M. Pietryga, V.I. Klimo, Nano Lett. **7**, 3469 (2007)
3. Y. Fu, Y.H. Zhou, H.B. Su, F.Y.C. Boey, H. Ågren, J. Phys. Chem. C **114**, 3743 (2010)
4. A. Luque, A. Marti, Phys. Rev. Lett. **78**, 5014 (1997)
5. L. Cuadra, A. Marti, A. Luque, Thin Solid Films **451–452**, 593 (2004)
6. M.A. Green, Prog. Photovolt. **9**, 137 (2001)
7. A. Luque, A. Marti, Prog. Photovolt. **9**, 73 (2001)
8. A. Luque, A. Marti, C. Stanley, N. Lopez, L. Cuadra, D. Zhou, J.L. Pearson, A. McKee, J. Appl. Phys. **96**, 903 (2004)
9. A. Marti, N. Lopez, E. Antolin, E. Canovas, A. Luque, C.R. Stanley, C.D. Farmer, P. Diaz, Appl. Phys. Lett. **90**, 233510(3) (2007)
10. E. Antolin, A. Marti, C.R. Stanley, C.D. Farmer, E. Canovas, N. Lopez, P.G. Linares, A. Luque, Thin Solid Films **516**, 6919 (2008)
11. A. Marti, E. Antolin, C.R. Stanley, C.D. Farmer, N. Lopez, P. Diaz, E. Canovas, P.G. Linares, A. Luque, Phys. Rev. Lett. **97**, 247701(4) (2006)
12. A. Luque, A. Marti, N. Lopez, E. Antolin, E. Canovas, C. Stanley, C.D. Farmer, L. Cuadra, J.L. Balenzategui, Appl. Phys. Lett. **87**, 083505(3) (2005)
13. V. Aroutiounian, S. Petrosyan, A. Khachatryan, J. Appl. Phys. **89**, 2268 (2001)
14. S.M. Hubbard, C.D. Cress, C.G. Bailey, R.P. Raffaelle, S.G. Bailey, D.M. Wilt, Appl. Phys. Lett. **92**, 123512(3) (2008)
15. X.J. Lu, J. Vaillancourt, M.J. Meisner, Semicond. Sci. Technol. **22**, 993 (2007)
16. W.H. Chang, T.M. Hsu, C.C. Huang, S.L. Hsu, C.Y. Lai, N.T. Yeh, J.I. Chyi, Phys. Status Solidi B **224**, 85 (2001)
17. S.M. Sze, *Semiconductor Devices: Physics and Technology* (Wiley, New Jersey, 1985)
18. A. Marti, L. Cuadra, A. Luque, IEEE Trans. Electron Devices **48**, 2394 (2001)
19. K. Takahashi, S. Yamada, T. Unno, Hitachi Cable Rev. **17**, 7 (1998)
20. X.-F. Yang, K. Fu, W. Lu, W.-L. Xu, Y. Fu, J. Phys. D, Appl. Phys. **42**, 125414(8) (2009)
21. Y. Fu, M. Willander, J. Appl. Phys. **71**, 3877 (1992)
22. Y. Hou, W.P. Wang, N. Li, W. Lu, Y. Fu, J. Appl. Phys. **104**, 074508(5) (2008)
23. H.Z. Song, S. Lan, K. Akahane, K.Y. Jang, Y. Okada, M. Kawabe, Jpn. J. Appl. Phys. **39**, 5746 (2002)